Journal of Materials Chemistry A

Accepted Manuscript

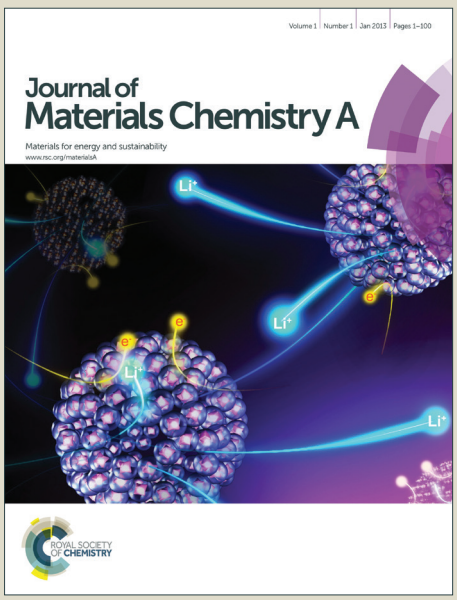

ROYAL SOCIETY OF CHEMISTRY

www.rsc.org/materialsA

Cite this: DOI: 10.1039/c0xx00000x

www.rsc.org/xxxxxx

ARTICLE TYPE

Interlaced $W_{18}O_{49}$ Nanofibers as Superior Catalyst for Counter Electrode of Highly Efficient Dye-Sensitized Solar Cells

Huawei Zhou[a], Yantao Shi[a,*], Qingshun Dong[a], Yanxiang Wang[b], Chao Zhu[c], , Liang Wang[a], Ning Wang[c], Ying Wei,[a] Shengyang Tao[a], Tingli Ma[a,d,*]

Received (in XXX, XXX) Xth XXXXXXXXX 20XX, Accepted Xth XXXXXXXXX 20XX

DOI: 10.1039/b000000x

Sufficient contact, high catalytic activity, free electron transport and ionic diffusion are desired for the liquid-solid heterogeneous electrocatalysis. However, preparing catalysts that simultaneously possess all these four advantages has proven challenging. Nanostructures originated from anisotropic growth always exhibit specific structural advantages and unique properties of physical, chemical or catalytic. Herein, *via* a facile and template-free approach of the solvothermal, we synthesized $W_{18}O_{49}$ nanofibers (NFs), nanofibers bundles (NFBs), as well as hierarchical spheres (HSs). As catalyst for the counter electrode (CE) of dye-sensitized solar cells (DSCs), $W_{18}O_{49}$ NFs demonstrated remarkable electrocatalytic activities because: (i) abundant oxygen vacancies offered sufficient active sites for reduction of I_3^- into I^-; (ii) one dimension NFs were more beneficial to electron transport; (iii) two phase, the liquid electrolyte and the solid NFs, could fully contacted and meanwhile ions could diffuse freely among the networks constructed by interlaced NFs. Notably, DSCs using the NF-based semitransparent CE achieved high photoelectric conversion efficiencies (PCEs) up to 8.58%, superior to that based on NFBs or HSs, and comparable to that of 8.78% using Pt as CE. Furthermore, it was proved that both the electrolytic activity and the PCEs deteriorated drastically when NFs were destructed. Our work here will be great interest for both fundamental research and practical applications of $W_{18}O_{49}$ nanomaterials in other fields.

Introduction

Dye-sensitized solar cells (DSCs), one of the most promising photovoltaic devices, are attractive to scientists and manufactures due to their unique advantages, such as relative low-cost, high efficiency, facile fabrication, colorization, etc.[1-3] Among the key components of DSCs, the counter electrode (CE), which is responsible for collection of electrons from external circuit and reduction of I_3^- into I^-, has been generally fabricated by depositing the notable metal platinum (Pt) on FTO conductive glass.[4] Consequently, replacing Pt with inexpensive but efficient catalyst is meaningful and has become one of the priorities in this field. Recent years, our papers, as well as those from other groups, have demonstrated the applications of inorganic materials for fabricating CEs of DSCs, including oxides,[5, 6] nitrides,[7-10] carbides,[11] sulfides,[12, 13] selenides[14], and phosphides.[15, 16] Of these materials, oxides are relatively stable, cost-effective, abundant in variety and facile in preparation.

To date, most of the oxides used as CEs for DSCs are nanoparticles (NPs) and their relevant photoelectric conversion efficiencies (PCEs) were 1.07% for Cr_2O_3, 5.40% for V_2O_3,[17] 6.0% for WO_2,[6] 6.96% for α-Fe_2O_3.[18] As we all know, sufficient contact, high catalytic activity, free electron transport and ionic diffusion are critical for the liquid-solid heterogeneous catalysis. In these NPs-based CEs, however, inter-particle boundaries are massive and seriously hinder the carrier transport. In the meantime, NPs tend to aggregate together, resulting in loss of the surface area. Thus at present, it is highly desired to develop superior catalytic materials that can satisfy all of these requirements. Due to the strong facets and shape dependent properties in nanoscale, anisotropic nanostructures usually exhibit unique properties such as electronic, magnetic and optical, attractive to scientists in the fields of catalysis, solar cells, light-emitting diodes, etc.[19-22] Transition metal oxides WO_{3-x} ($0 \leqslant x \leqslant 1$) have wide practical applications.[23, 24] Among tungsten oxides, $W_{18}O_{49}$ has strong anisotropic growth behavior along [010] direction. Resultant one dimensional (1D) $W_{18}O_{49}$ nanowires (NWs) or nanorods (NRs) in turn have massive surface oxygen vacancies.[25-28] In addition, $W_{18}O_{49}$ has high charge carrier density and has opened up many practical applications in the areas of electrochromic windows, secondary batteries, optical devices, gas sensors, and photocatalysts.[29] Recently, Ye et al. found that ultrathin $W_{18}O_{49}$ NWs were efficient in the photochemical reduction of carbon dioxide.[25] Guo et al. also employed $W_{18}O_{49}$ nanorods (NRs) to transmit visible light and absorb near- infrared light.[26] Up to date, research on using one dimensional $W_{18}O_{49}$ nanostructures for CE fabrication has been merely reported in the field of DSCs.

Herein, via a template-free solvothermal route, we reported the preparation of anisotropic-growth-induced 1D $W_{18}O_{49}$ nanofibers (NFs), self-assembled nanofiber bundles (NFBs), as well as

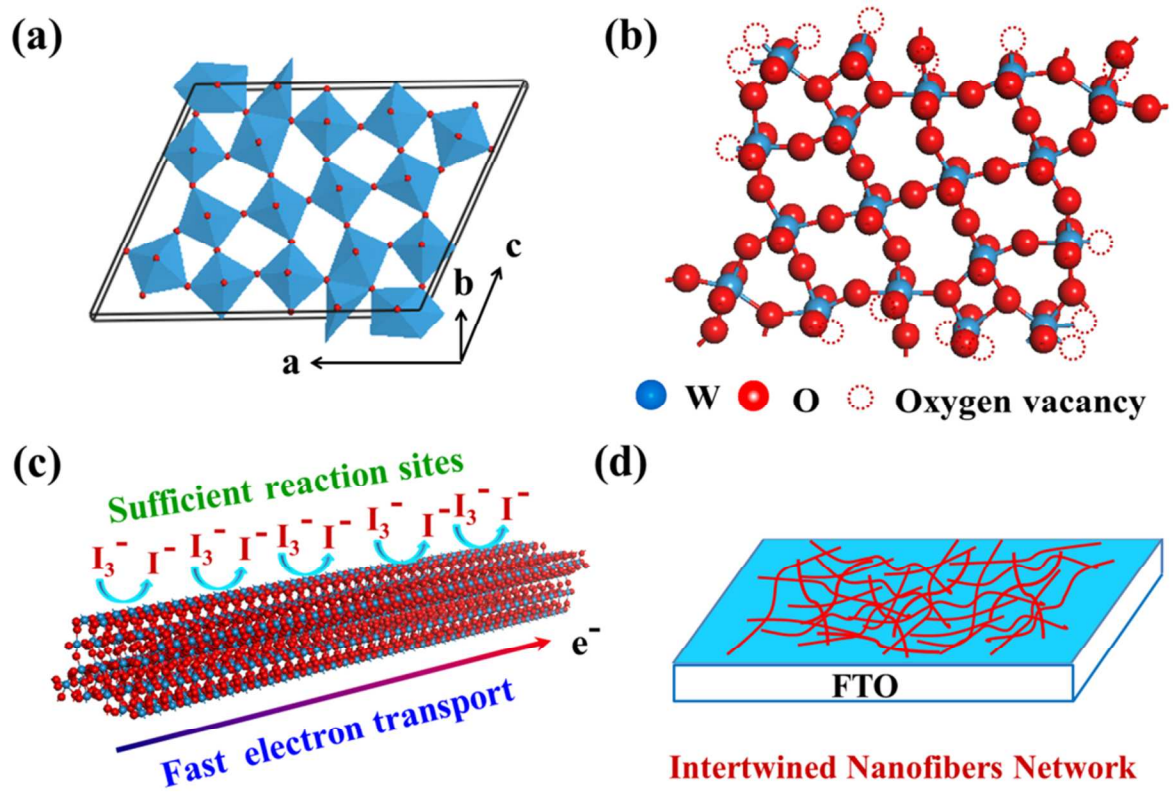

Scheme 1. (a) and (b) Unit cell structure and atomic arrangements of the $W_{18}O_{49}$; (c) schematic showing facilitated catalytic reaction and fast electron transport along one dimensional $W_{18}O_{49}$ nanostructures; (d) schematic of the counter electrode based on interlaced $W_{18}O_{49}$ nanofibers.

hierarchical spheres (HSs). As demonstrated in Scheme 1, structural advantages of $W_{18}O_{49}$ NFs enabled these nanostructures to be superior catalyst as the CE for DSCs. Firstly, unique crystal structure offers abundant oxygen vacancies as active sites for reduction of I_3^- into I^-. Secondly, one dimension NFs are more beneficial to electron transport. Thirdly, two phase, the liquid electrolyte and the solid NFs, can fully contacted and meanwhile ions could diffuse freely among the networks constructed by interlacing of NFs. Notably, DSCs using the NF-based, semitransparent CE achieved high PCEs up to 8.58%, superior to that based on NFBs or HSs, and comparable to that of 8.78% using Pt as CE. Furthermore, it was proved that both the electrolytic activity and the PCEs deteriorated drastically when NFs were destructed.

Experimental Section

Synthesis: In a typical procedure, a certain amount of WCl_6 was dissolved in 50 mL ethanol to form clear yellow solution that was then transferred into a Teflon-lined autoclave. After being heated at 180 °C for 24 h, the mixture was cooled to room temperature naturally. The product was collected by centrifugation and washed repeatedly with water and ethanol, finally followed by vacuum drying at 45°C overnight.

Preparation of CEs: As-synthesized $W_{18}O_{49}$ powders (10 mg) were dispersed in isopropanol (3 mL). Then obtained suspension (0.5 ml) was sprayed on FTO glass (0.8 cm × 10 cm). The obtained films was sintered in nitrogen atmosphere at 500 °C for 30 min. Noble metal Pt CEs were fabricated by pyrolysis H_2PtCl_6 on FTO glass as previously reported.[34, 35]

Solar cell fabrication: A layer of 20 nm-sized TiO_2 (P25, Degussa, Germany) layer (12 μm) was printed on FTO glass. When the obtained films sintered at 500 °C were cooled to 90 °C, they were immersed in a solution of N719 dye (5 x 10^{-4} M) in acetonitrile/tert-butyl alcohol (1:1 volume ration) for 22 h. The electrolyte for solar cell was composed of LiI (0.03 M), 1-butyl-3-methylimidazolium iodide (0.6 M), I_2 (0.03 M), 4-tert-butyl pyridine (0.5 M), guanidinium thiocyanate in acetonitrile (0.1 M). The architecture of DSCs was assembled by sandwiching electrolyte with a sensitized TiO_2 photoanode and a counter electrode.

Characterizations: XRD patterns were obtained using PANalyticalX´Pert diffractometer (Cu Kα radiation at λ = 1.54 Å) sampling at 2°/ min, 40 kV and 100 mA. Nanostructures of our samples were characterized and analyzed by scanning electron microscopy (SEM, Nova Nano SEM 450), transmission electron microscopy (TEM, FEI Tecnai G2 F30). UV/Vis/NIR absorption spectrum was obtained using UV/Vis/NIR spectrometer (Perkinelmer, lambda, 750S). The films thicknesses were measured using film-thickness measuring device (Surfcom 130A, Japan). The photocurrent–voltage performance of the DSCs was measured by a Keithley digital source meter (Keithley 2601, USA) equipped with a solar simulator (PEC-L15, Peccell, Yokohama, Japan). EIS experiments were measured in the dummy cells in the

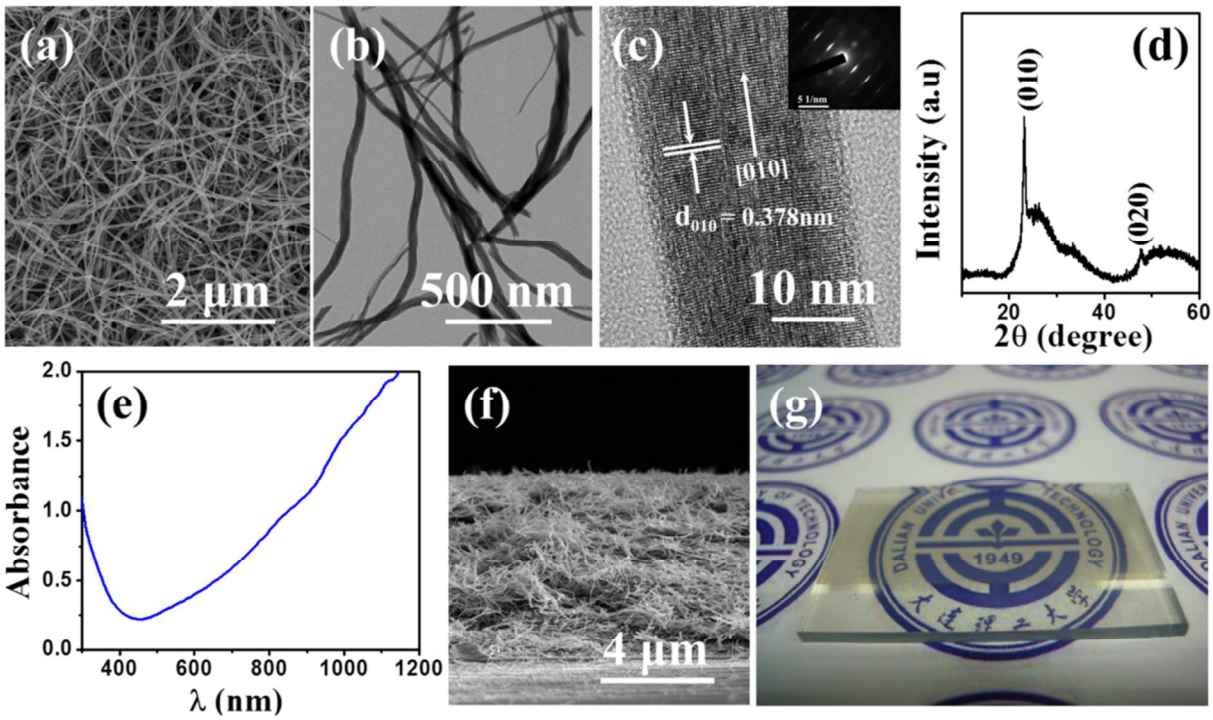

Figure 1. (a) SEM image of the interlaced $W_{18}O_{49}$ NFs; (b) and (c) TEM images of the $W_{18}O_{49}$ NFs, the insert in (c) is selected area electron diffraction pattern; (d) XRD pattern of the $W_{18}O_{49}$ NFs; (e) UV/Vis/NIR absorption spectra of $W_{18}O_{49}$ NFs. (f) cross-sectional SEM image of film composed of $W_{18}O_{49}$ NFs; (g) a photo showing the semitransparency of our CE based on $W_{18}O_{49}$ NFs.

dark using a computer-controlled potentiostat (ZenniumZahner, Germany). Tafel polarization measurements were carried out with an electrochemical workstation system (CHI630, Chenhua, and Shanghai) in a symmetrical dummy cell. Effective area of the symmetrical cells in the EIS and Tefal-polarization tests was 0.64 cm^2.

Results and Discussions

Our $W_{18}O_{49}$ NFs were prepared *via* the solvothermal that was conducted by heating the sealed mixture of 0.10 g WCl_6 and 50 ml ethanol at 180 ^oC for 24 hours. Obtained product was designated as sample 1. Scanning electron microscopic (SEM) image in Figure 1a clearly illustrates the morphology of sample 1, in which massive NFs are densely and randomly interlaced together, thus offering a desired network structure for subsequent heterogeneous catalytic reaction. It can be found in Figure 1a that aspect ratios of these bent 1D nanostructures are generally high. Since no surfactant or shape-guiding agent was applied in our synthesis, preferred growth along one specific direction dominated the final shape of the NFs. Lengths of some long NFs nearly approach 4 μm while their diameters are well confined within the range from 10 nm to 65 nm (see the enlarged SEM image in Figure S1). Our inhomogeneity NFs with large aspect ratios are also illustrated by transmission electron microscopy (TEM) image in Figure 1b. In addition, the high resolution TEM (HRTEM) image and corresponding selected area electron diffraction (SAED) of a NF (with a diameter of *ca.* 30 nm) are shown in Figure 1c, in which the interplanar *d*-spacing is approximately 0.378 nm, in good agreement with that of the monoclinic $W_{18}O_{49}$ along [010] direction. Among tungsten oxides, $W_{18}O_{49}$ usually exhibits anisotropic growth along [010], thus tending to form 1D nanostructures. For some NFs, however, the stacking faults exist in the direction perpendicular to [010], as demonstrated in Figure S2. Thus it can hardly be said that all of our NFs are perfect monocrystalline. This finding is similar with previous report. X-ray diffraction (XRD) pattern in Figure 1d further confirms the phase of our NFs to be monoclinic $W_{18}O_{49}$ since all peaks can be well assigned according to Joint Committee on Powder Diffraction Standards Cards (No. 71-2450). Actually, $W_{18}O_{49}$ nanostructures have been reported many times in one-dimensional forms like nanorods and nanofibers, even without using shape-guiding agents.[25, 26] We all know that WO_6 octahedron is one kind of basic unit in tungsten oxides. According to the chemical bonding theory of single crystal growth, the fastest growth rate can be achieved by linking WO_6 octahedra to form linear rows.[30, 31] Fig. 1a shows the $W_{18}O_{49}$ unit cell structure, in which the WO_6 octahedra attach to each other in a complex way by sharing corners and edges. Obviously, compared with another two directions, it is much easier to grow along b axis since these WO_6 octahedra can be linked as linearly as possible.

As well known, structure-dependent properties in level of nanoscale are of great significance for nowadays photochemical or photovoltaic devices. Sufficient contact, high catalytic activity, free electron transport and ionic diffusion are desired for liquid-solid heterogeneous catalysis. Fortunately, our $W_{18}O_{49}$ NFs can be regarded as ideal nanomaterial in terms of satisfying these four criteria simultaneously. These NFs have large surface area exposed and more importantly the nonstoichiometric $W_{18}O_{49}$

Table 1. Photovoltaic parameters of the DSCs from the *J-V* curves shown in Figure 3 and EIS parameters of the symmetrical cells based on these CEs

CE	V_{oc} (V)	J_{sc} (mA cm^{-2})	FF	PCE (%)	R_s (Ω)	R_{ct} (Ω)	Z_N (Ω)
NFs	0.70	17.14	0.66	7.94	14.52	0.98	4.51
NFBs	0.71	17.08	0.63	7.66	15.42	1.18	6.12
HSs	0.71	16.50	0.53	6.20	14.24	29.12	7.56
Pt	0.70	16.69	0.68	8.01	9.73	3.30	2.73

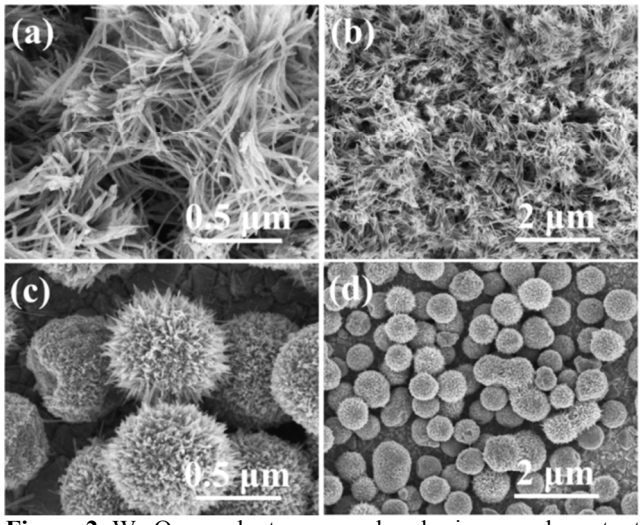

Figure 2. $W_{18}O_{49}$ products prepared under increased reactant concentration: (a) and (b) sample 2, synthesized in 0.17 g WCl_6 in 50 ml ethanol; (c) and (d) sample 3 synthesized in 0.50 g WCl_6 in 50 ml ethanol.

itself can offer massive oxygen deficiencies, as evidenced by ultraviolet/visible/near infrared (UV/Vis/NIR) absorption spectroscopy in Figure 1e. According to previous reports, the large absorption tail extending from visible to near infrared (NIR) range is thought to be closely related to the free electrons and oxygen-vacancy-induced small polarons.[25-28] Undoubtedly, with these oxygen vacancies our $W_{18}O_{49}$ NFs can offer abundant active sites for catalytic reaction. In terms of charge transport, electrons are able to travel freely along these long 1D $W_{18}O_{49}$ nanostructures as well as their interlaced networks, instead of being scattered repeatedly by grain boundaries of particulate nanostructures. Furthermore, broad spacing or channels among these $W_{18}O_{49}$ NFs, as illustrated either by top-view SEM image in Figure 1a or the cross-sectional one in Figure 1f, are advantageous for pore-filling and ionic diffusion. Finally, when $W_{18}O_{49}$ NFs were sprayed onto FTO glass, the as-fabricated CE shown in Figure 1g was semi-transparent.

For better understanding the superiorities of NFs in subsequent photovoltaic devices, we prepared another two differently structured samples for systematic comparison. In synthesis of

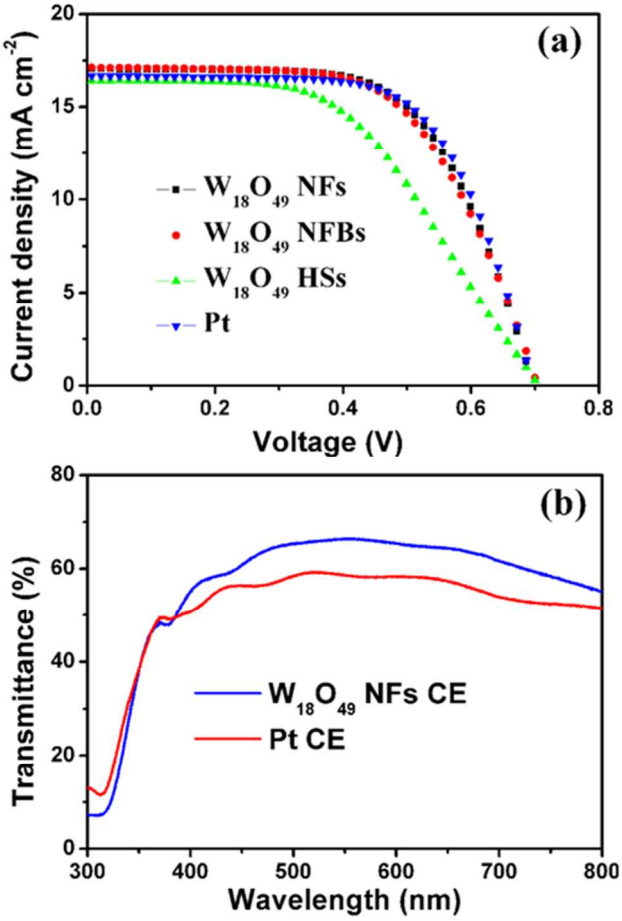

Figure 3. (a) *J-V* curves of DSCs based on different CEs; (b) transmittances of $W_{18}O_{49}$ NFs-based CE and Pt CE.

aforementioned sample 1, WCl_6 contained in 50 ml ethanol was only 0.10 g. When slightly increasing WCl_6 from 0.10 g to 0.17 g, sample 2 was obtained and differed a lot from sample 1 in morphology. Rather than these randomly interlaced NFs in sample 1, NFs in sample 2 were inclined to be loosely bundled together by self-assembled, as shown in Figure 2a and 2b. Compared sample 1, dimensions of these NFs bundles (NFBs) in sample 2 however are largely decreased to below 1 μm. Sample 3 was prepared by increasing WCl_6 to 0.5 g, products shown in Figure 2c are submicron 3D hierarchical spheres (HSs) in which

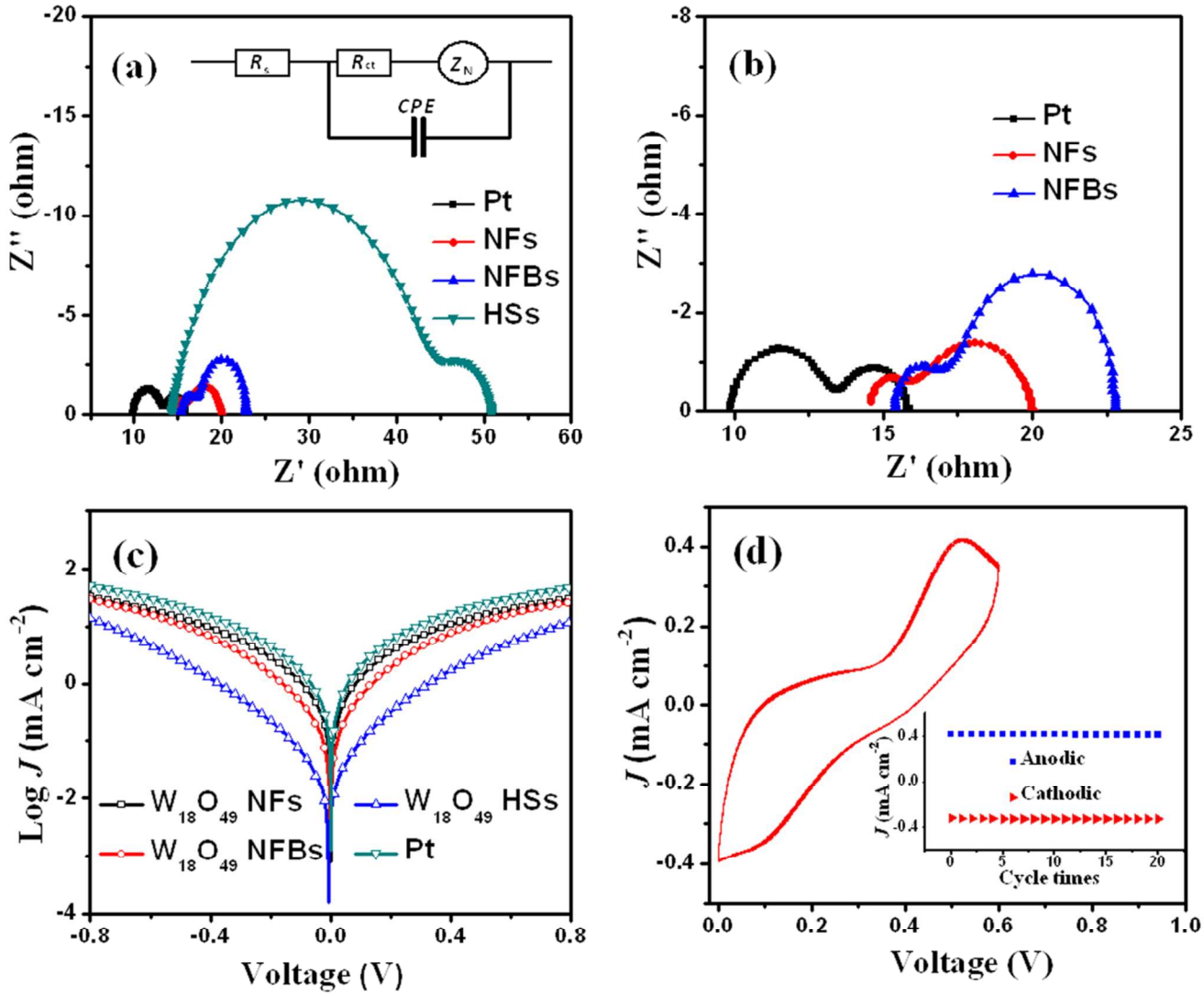

Figure 4. Electrochemical characterizations. Part I: measurements of the symmetrical cells fabricated with two identical CEs, (a) and (b) Nyquist plots displayed at different ranges; (c) Tafel curves. Part II: 20 consecutive CVs of the $W_{18}O_{49}$ NFs-based CE in electrolyte solution containing 2 mM LiI, 0.02 mM I_2, and 20 mM $LiClO_4$; anodic and cathodic peak current densities versus cycle times (the inset).

some NFs outstretch, as sea urchin. Crystal phase of these two samples were also identified as monoclinic $W_{18}O_{49}$ by XRD results (Figure S3). We can find that, as the increase of precursor concentration, $W_{18}O_{49}$ NFs are decreased in length and apt to aggregate together. BET measurements performed in our work revealed the specific areas of 43.30 $m^2 g^{-1}$, 60.80 $m^2 g^{-1}$ and 69.94 $m^2 g^{-1}$ for NFs, NFBs and HSs, respectively. This trend could be probably ascribed to the decreased length of NFs in these three samples. The low magnification SEM images of morphology of $W_{18}O_{49}$ synthesized in corresponding concentration were provided in Figure S4, S5, and S6.

By spraying onto FTO glass, these three samples were fabricated into CEs and meanwhile traditional Pt CE was used as reference. To start with, photocurrent density-voltage (J–V) curves were obtained by characterizing these DSCs under AM 1.5, 100 mW cm^{-2} simulated illumination, as demonstrated in Figure 3a. The detailed photovoltaic parameters are summarized in Table 1. We can found that the DSCs based on $W_{18}O_{49}$ NFs gave PCEs of 7.94%, the highest one among these three samples and nearly approaching that of 8.01% based on Pt CE. Although nanostructures in sample 2 were $W_{18}O_{49}$ NFBs, no obvious changes were observed for open-circuit voltage (V_{oc}) and short-circuit current density (J_{sc}) for the corresponding DSCs. Thus, for NFBs-based DSCs, the slight decrease in PCEs from 7.94% to 7.66% could be attributed to the decreased fill factor (*FF*). When using $W_{18}O_{49}$ HSs-based CE, deterioration in FF (from 0.63 to 0.53) of the DSCs became more pronounced and finally resulted in a relative low PCEs of 6.20%. We all know that nanostructures of CEs in such electro-catalytic system are vital to catalytic reaction, ionic diffusion and electron transport, in turn greatly affecting the *FF* of DSCs. Hence, it is necessary to carry out investigations to reveal the relationships between CEs nanostructures and DSCs performances. In addition, as shown in

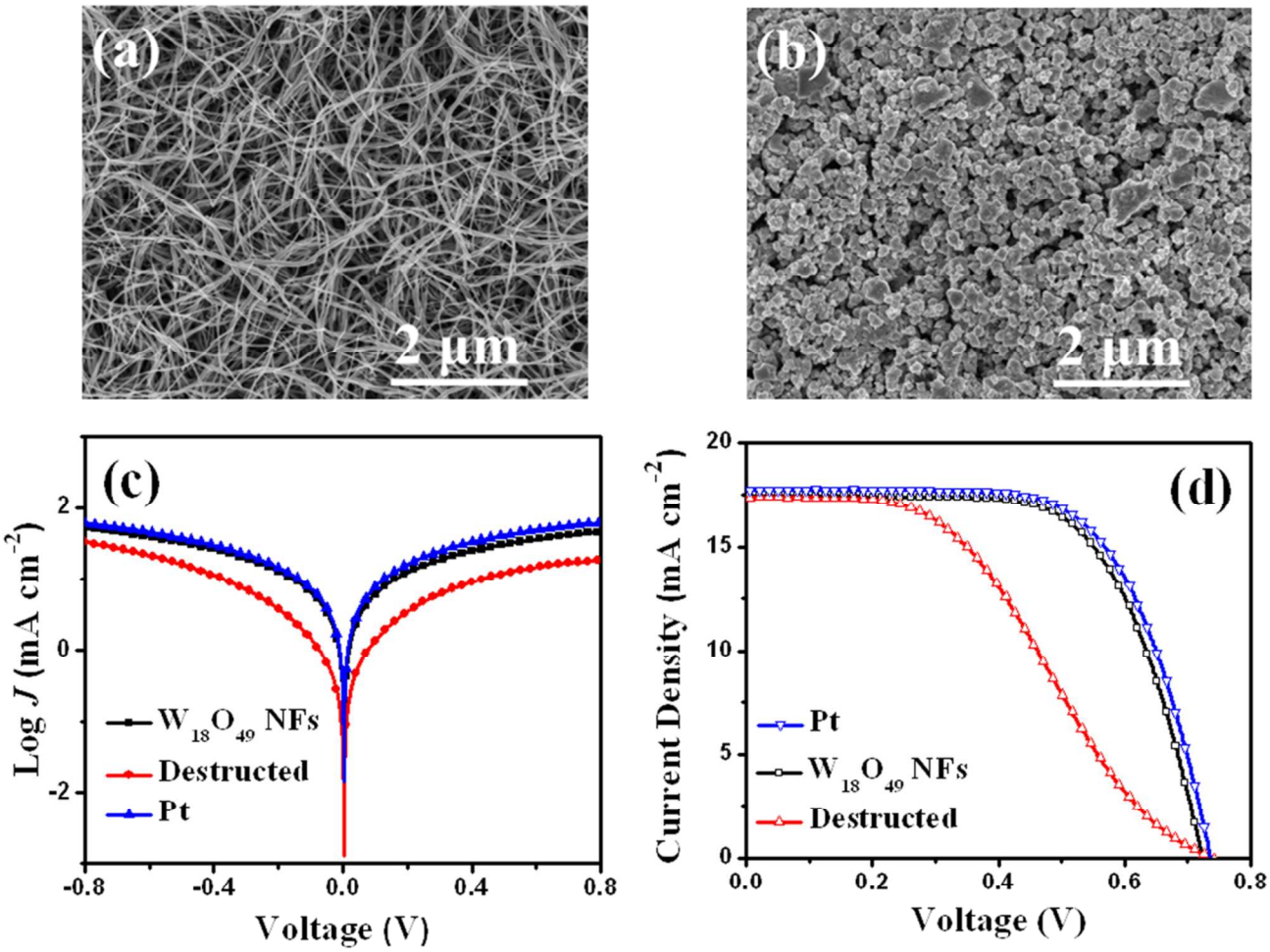

Figure 5. SEM image of $W_{18}O_{49}$ NFs: (a) original and (b) destructed by grinding; Tafel (c) curves of the symmetric cells of original $W_{18}O_{49}$ NFs and destructed one by grinding; *J-V* (d) curves of the relevant DSCs devices based on of original $W_{18}O_{49}$ NFs and destructed one by grinding.

Figure 3b, we compared the light transmittance and found that $W_{18}O_{49}$ NFs-based CEs was superior to Pt-based CE. It can be regarded as another advantage of using our $W_{18}O_{49}$ NFs as CE since the high transmittance can meet the demand to allow for fabrication of mechanically stacked DSCs tandems, partially transparent DSCs for building integration, and DSCs based on metal foil substrates.

Electrochemical methods of electrochemical impendence spectroscopy (EIS), Tafel-polarization, and cyclic voltammetry (CV) were used to reveal the inherent mechanism by which nanostructures affect the catalytic reaction and the performance of DSCs. Under the condition of dark, EIS measurements were performed with symmetrical cells consisting of two identical CEs. The results are shown in Figure 4a and 4b, meanwhile, an equivalent circuit diagram (the insert in Figure 4a) is provided for fitting Nyquist plots with the well-known software, the "Z-view".[13, 32] Each plot is composed of two irregular semicircles, among which the first one arises from the charge transfer resistance R_{ct} (for I_3^- reduction) at the CE/electrolyte interface. The second semicircle is derived from the Nernst diffusion impedance (Z_N) of I_3^-/I^- within electrolyte. Besides, value of the real part of Nyquist plot at the starting point (or intercept on the real axis) corresponds to the series resistance R_s. Fitting results of Nyquist plots are listed in Table 1, from which we can easily find that R_s values for our three $W_{18}O_{49}$ samples are almost the same but larger than that of Pt CE. R_{ct} of 0.98 Ω and 1.18 Ω for CEs based on NFs and NFBs, however, are obviously smaller than that of 3.30 Ω for Pt CE. For samples 1 and 2, such good catalytic activities are highly relevant to their structural advantages, e.g. interlaced network, large specific area, abundant reaction sites, and thorough contact with the electrolyte solution. By contrast, the catalytic activity of HSs-based CE is quite unsatisfactory since its R_{ct} of 29.12 Ω is far beyond that of another three CEs. As aforementioned, of these three $W_{18}O_{49}$ samples, HSs of sample 3 has the largest specific area of 69.94 m^2 g^{-1}. Thus accordingly, its catalytic activity is supposed to be better if the surface is fully utilized for catalytic reaction. Returning to SEM images in Figure 2, we may find out some limiting factors to the electrolytic activity of sample 3. As we know, fast carrier transport is preferred for heterogeneous electrocatalysis. Unlike NFs CEs in which electrons could transport freely along the

Table 2. Photovoltaic parameters of the DSCs based on $W_{18}O_{49}$ NFs, destructed $W_{18}O_{49}$ NFs and Pt CEs

CE	V_{oc}/ V	J_{sc}/ mAcm^{-2}	FF	PCE/%
$W_{18}O_{49}$ NFs	0.73	17.39	0.68	8.58
After grinding	0.73	17.59	0.41	5.26
Pt	0.74	17.65	0.67	8.78

interlaced NFs network, in HSs slow electron transport owing to the deficient contact between adjacent HSs may be regarded as one possible reason for its relative poor catalytic performance. Besides, in HSs the NFs are tightly aggregated together, thus electrolyte solution tends to be confined within the tiny pores and ionic diffusion will slow down. Because of that, Z_N for HSs-based CE was larger than that of Pt CE and another two.

Using the same symmetrical cells as in the case of EIS, Tafel curves were obtained by plotting polarization current (Log *J*) as a function of applied potential (U).[33] In Figure 4c, the limiting diffusion zone at the high potential arises from ionic diffusion of triiodide (I_3^-) and iodide (I^-) in the electrolyte. The sharp decrease at the middle potential is the Tafel zone, corresponding to charge transfer between I_3^- and CE. For HSs, current densities stemming from both ionic diffusion and charge transfer are obvious smaller than that of Pt and another $W_{18}O_{49}$ samples, in good accordance with EIS measurements. In this work, by means of consecutive CV measurements, we also elucidated how stable our NFs-based CE was in electrolyte solution. As can be found in Figure 4d, 20 CV curves coincide very well, indicating that our $W_{18}O_{49}$ NFs-based CE has a good stability under the practical working conditions. To study whether there was destruction or corrosion of $W_{18}O_{49}$ during the reaction at counter electrode, we immersed $W_{18}O_{49}$ CEs in electrolyte of DSSCs for 48 h and then characterized it with SEM. As shown in Fig. S8, no obvious destruction was observed for $W_{18}O_{49}$ NFs after immersing treatment.

Based on above characterizations and discussions, for these three $W_{18}O_{49}$ samples we believe it was the nanostructure-dependent electrocatalytic activity that mainly determined *FF* and final PCE of DSCs. Undoubtedly, as CE material for liquid-solid heterogeneous electrocatalysis in DSCs, the interlaced $W_{18}O_{49}$ NFs network is the most ideal nanostructure among our samples since it can well satisfy these criteria like sufficient contact, high catalytic activity, free electron transport and ionic diffusion. For further proving the importance of this nanostructure, we thoroughly destructed $W_{18}O_{49}$ NFs on purpose. As demonstrated in Figure 5a and 5b, after 30 min grinding our original NFs changed into aggregated particles and meanwhile the specific area was drastically decreased to 8.5 m^2 g^{-1}. We can easily observe that the destructed NFs almost lost all structural advantages. Tafel curves in Figure 6a suggests that the charge-transfer current of the CE based on destructed NFs is far below that of the one based on the un-destructed. On the other hand, EIS result (Figure S7) also indicated the severely lowered electrocatalytic activity since the R_{ct} increased from 0.98 Ω to 15.42 Ω after $W_{18}O_{49}$ NFs being destroyed. J-V measurements were conducted subsequently and detailed parameters are summarized in Table 2. After destruction, decreases in FF from 0.68 to 0.41 and in PCE from 8.58% to 5.26% were extremely serious. Under the same condition, PCE of DSCs based on Pt CE was 8.78%. Once again, above results confirmed that our $W_{18}O_{49}$ NFs was comparable to Pt as CEs for DSCs.

Conclusions

In summary, using the solvothermal route we reported the preparations of three $W_{18}O_{49}$ nanostructures, 1D $W_{18}O_{49}$ NFs induced by anisotropic growth, self-assembled NFBs, as well as HSs. As the CE for DSCs, these interlaced $W_{18}O_{49}$ NFs offered a desired network structure for heterogeneous electro-catalysis and exhibited multi-superiorities by offering abundant active sites, interlaced highways for electron transport and broad pore structures for thorough contact with electrolyte solution. Systematic comparisons were conducted to reveal the influence of nanostructure on electrocatalytic activity. Notably, our semi-transparent $W_{18}O_{49}$ NFs CEs enabled the DSCs to achieve a high PCE of 8.58%, quite close to that of 8.78% for the Pt-based and can be regarded as an ideal material for catalytic reaction in DSCs. It is believed that such materials and nanostructures will be of great interest to researches of other fields.

Acknowledgements

This work was financially supported by National Natural Science Foundation of China (Grant no.51273032), National High Technology Research and Development Program for Advanced Materials of China (Grant no.2009AA03Z220), Specialized Research Fund for the Doctoral Program of Higher Education of China (20110041110003), Open project of the State Key Laboratory for Physical Chemistry of Solid Surfaces of Xiamen University (Grant no. 201210), the Fundamental Research Funds for the Central Universities (Grant No. DUT12RC(3)57), International Science & Technology Cooperation Program of China (Grant No. 2013DFA51000) and the State Key Laboratory of Fine Chemicals of Dalian University of Technology.

Notes and references

[a] *State Key laboratory of Fine Chemicals, School of Chemistry, Dalian University of Technology, Dalian, China.*
[b] *School of Material Science and Engineering, JingDeZhen Ceramic Institute, JingDeZhen, China.*
[c] *Department of Physics, the Hong Kong University of Science and Technology, Hong Kong, China.*
[d] *Graduate School of Life Science and Systems Engineering, Kyushu Institute of Technology, 2-4 Hibikino, Wakamatsu, Kitakyushu, Fukuoka, 808-0196, Japan.*
* *Corresponding authors: tinglima@dlut.edu.cn; shiyantao@dlut.edu.cn*

Electronic Supplementary Information (ESI) available: XRD patterns of the $W_{18}O_{49}$ NFBs and HSs. The low magnification images for $W_{18}O_{49}$ nanostructures. The HRTEM image of $W_{18}O_{49}$ NFs. Nyquist plots of the symmetrical cells fabricated with the destructed $W_{18}O_{49}$ NFs. See DOI: 10.1039/b000000x/

1. B. Oregan and M. Gratzel, *Nature*, 1991, **353**, 737-740.
2. L. Kavan, J.-H. Yum and M. Graetzel, *Nano Lett.*, 2011, **11**, 5501-5506.
3. E. J. W. Crossland, M. Nedelcu, C. Ducati, S. Ludwigs, M. A. Hillmyer, U. Steiner and H. J. Snaith, *Nano Lett.*, 2009, **9**, 2813-2819.
4. A. Yella, H.-W. Lee, H. N. Tsao, C. Yi, A. K. Chandiran, M. K. Nazeeruddin, E. W.-G. Diau, C.-Y. Yeh, S. M. Zakeeruddin and M. Graetzel, *Science*, 2011, **334**, 629-634.

5. X. Lin, M. Wu, Y. Wang, A. Hagfeldt and T. Ma, *Chem. Commun.*, 2011, **47**, 11489-11491.
6. M. Wu, X. Lin, A. Hagfeldt and T. Ma, *Chem. Commun.* 2011, **47**, 4535-4537.
7. E. Ramasamy, C. Jo, A. Anthonysamy, I. Jeong, J. K. Kim and J. Lee, *Chem. Mater.*, 2012, **24**, 1575-1582.
8. G.-r. Li, F. Wang, Q.-w. Jiang, X.-p. Gao and P.-w. Shen, *Angew. Chem., Int. Ed.* 2010, **49**, 3653-3656.
9. Q. W. Jiang, G. R. Li and X. P. Gao, *Chem. Commun.*, 2009, 6720-6722.
10. G. R. Li, J. Song, G. L. Pan and X. P. Gao, *Energy. Environ. Sci.*, 2011, **4**, 1680-1683.
11. M. Wu, X. Lin, A. Hagfeldt and T. Ma, *Angew. Chem., Int. Ed.* 2011, **50,** 3520-3524.
12. L. Yi, Y. Liu, N. Yang, Z. Tang, H. Zhao, G. Ma, Z. Su and D. Wang, *Energy. Environ. Sci.* 2013, **6**, 835-840.
13. H. Sun, D. Qin, S. Huang, X. Guo, D. Li, Y. Luo and Q. Meng, *Energy. Environ. Sci.*, 2011, **4**, 2630-2637.
14. X. Zeng, W. Zhang, Y. Xie, D. Xiong, W. Chen, X. Xu, M. Wang, Y. Cheng, *J. Power Sources,* 2013, 226, 359–362
15. Y. Y. Dou, G. R. Li, J. Song and X. P. Gao, *Phys. Chem. Chem. Phys.*, 2012, **14**, 1339-1342.
16. M. Wu, J. Bai, Y. Wang, A. Wang, X. Lin, L. Wang, Y. Shen, Z. Wang, A. Hagfeldt and T. Ma, *J. Mater. Chem.* 2012, **22**, 11121-11127.
17. M. Wu, X. Lin, Y. Wang, L. Wang, W. Guo, D. Qu, X. Peng, A. Hagfeldt, M. Graetzel and T. Ma, *J. Am. Chem. Soc.* 2012, **134**, 3419-3428.
18. Y. Hou, D. Wang, X. H. Yang, W. Q. Fang, B. Zhang, H. F. Wang, G. Z. Lu, P. Hu, H. J. Zhao and H. G. Yang, *Nat. Commun.* 2013, **4**.
19. E. Formo, E. Lee, D. Campbell and Y. Xia, *Nano Lett.* 2008, **8**, 668-672.
20. M. Law, L. E. Greene, J. C. Johnson, R. Saykally and P. D. Yang, *Nat. Mater.* 2005, **4**, 455-459.
21. B. D. Yuhas and P. Yang, *J. Am. Chem. Soc.* 2009, **131**, 3756-3761.
22. Q. Fang, S. Gradecak, L. Yat, W. Cheng-Yen and C. M. Lieber, *Nano Lett.* 2005, **5**, 2287-2291.
23. K. Manthiram and A. P. Alivisatos, *J. Am. Chem. Soc.* 2012, **134**, 3995-3998.
24. J. Polleux, A. Gurlo, N. Barsan, U. Weimar, M. Antonietti and M. Niederberger, *Angew. Chem., Int. Ed.* 2005, **45**, 261-265.
25. G. Xi, S. Ouyang, P. Li, J. Ye, Q. Ma, N. Su, H. Bai and C. Wang, *Angew. Chem., Int. Ed.* 2012, **51**, 2395 –2399.
26. C. Guo, S. Yin, M. Yan, M. Kobayashi, M. Kakihana and T. Sato, *Inorg. Chem.* 2012, **51**, 4763−4771.
27. B. W. Faughnan, R. S. Crandall and P. M. Heyman, *Rca Rev.* 1975, **36**, 177-197.
28. O. F. Schirmer, V. Wittwer, G. Baur and G. Brandt, *J. Electrochem. Soc.* 1977, **124**, 749-753.
29. H. Zheng, J. Z. Ou, M. S. Strano, R. B. Kaner, A. Mitchell and K. Kalantar-zadeh, *Adv. Funct. Mater.* 2011, **21**, 2175–2196.
30. X. Zhao, Z. Bao, C. Sun, D. Xue, *J. Cryst. Growth.* 2009, **311**, 711-715.
31. X. Yan, D. Xu, D. Xue, *Acta Mater.* 2007, 55, 5747-5757.
32. Q. Wang, J. E. Moser and M. Gratzel, *J.Phys. Chem. B.* 2005, **109**, 14945-14953.
33. M. Wang, A. M. Anghel, B. Marsan, N.-L. C. Ha, N. Pootrakulchote, S. M. Zakeeruddin and M. Graetzel, *J. Am. Chem. Soc.* 2009, **131**, 15976-15977.
34. N. Papageorgiou, W. F. Maier and M. Gratzel, *J. Electrochem. Soc.* 1997, **144**, 876-884.
35. G. Q. Wang, R. F. Lin, Y. Lin, X. P. Li, X. W. Zhou and X. R. Xiao, *Electrochim. Acta* 2005**, 50**, 5546-5552.

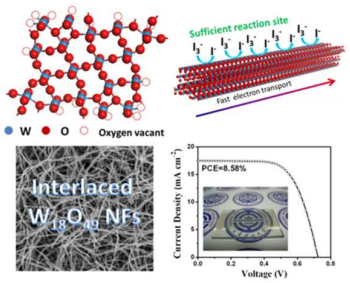

Interlaced $W_{18}O_{49}$ Nanofibers as Superior Catalyst for Counter Electrode of Highly Efficient Dye-Sensitized Solar Cells